

Quantitative Analysis of Third-harmonic Neutral-point Current, its Impacts, and Mitigation in Three-level NPC Inverters

D. Venkatramanan[†], V. Nimesh^{*}, Brian Johnson^{*}, and Sairaj Dhople[†]

[†]Department of Electrical and Computer Engineering, University of Minnesota, Minneapolis, MN 55414

^{*}Department of Electrical and Computer Engineering, University of Washington, Seattle, WA 98195

Emails: {dvenkat, sdhople}@umn.edu, {nimeshv, brianbj}@umw.edu

Abstract—Three-level neutral-point clamped inverter (3L-NPCI) is a widely popular topology in the realm of multi-level inverters. The low frequency third-harmonic neutral-point (NP) current in a 3L-NPCI and the corresponding NP-voltage oscillations on the DC-side are known characteristics of the 3L-inverter. In this paper, a quantitative analysis is presented for characterizing the DC-side third-harmonic phenomena observed in 3L-NPCI. Departing from the traditional space-vector perspective, an alternate formulation based on time-domain functions and Fourier-series is adopted, and an analytical expression for the 3rd harmonic NP-current is derived as a function of inverter modulation index and load power factor—this is applicable for all conventional carrier-based PWM techniques employed on 3L-NPCIs. The corresponding NP-voltage variation on the DC-side and its translation onto the AC-side as low-frequency harmonic distortions in the inverter output voltage are analytically quantified. Based on this, a model-based observer is designed to mitigate the AC side distortions through accurate estimation of the disturbance variables and feed-forward cancellation. Experimental results along with a full-order switched model simulation of a three-phase 3L-NPCI system validate the theoretical analysis and mitigation technique proposed in this paper.

I. INTRODUCTION

The pulse-width modulated (PWM) voltage-source inverter (VSI) is a vital component extensively used in several DC-AC power conversion applications such as grid-integration of photovoltaic systems, motor drives, and energy-storage systems [1]–[5]. In the realm of multilevel PWM VSIs, a three-level (3L) neutral-point clamped inverter (NPCI) is a widely popular topology [6], [7]. The reasons for its wide deployment are its superior performance characteristics in terms of PWM output-voltage quality and overall efficiency that are achieved with lower number of switches and at relatively low operational complexity [8], [9]. The circuit schematic of the R-phase leg of a three-phase T-type 3L-NPCI and a traditional 2L-VSI with pole current i_i^R are shown in Fig. 1 along with the corresponding PWM switching functions S_{S1} , S_{S2} and averaged duty-ratios d_+^R , d_-^R (complementary switching functions for the neutral-point devices not shown). The 3L-NPCI has the same set of active-states ($+0.5V_{dc}$, $-0.5V_{dc}$) as that of a 2L-VSI. The introduction of the third zero-state in case of 3L-NPCI, while leading to several performance benefits, also introduces additional power-circuit behaviors that are not observed in

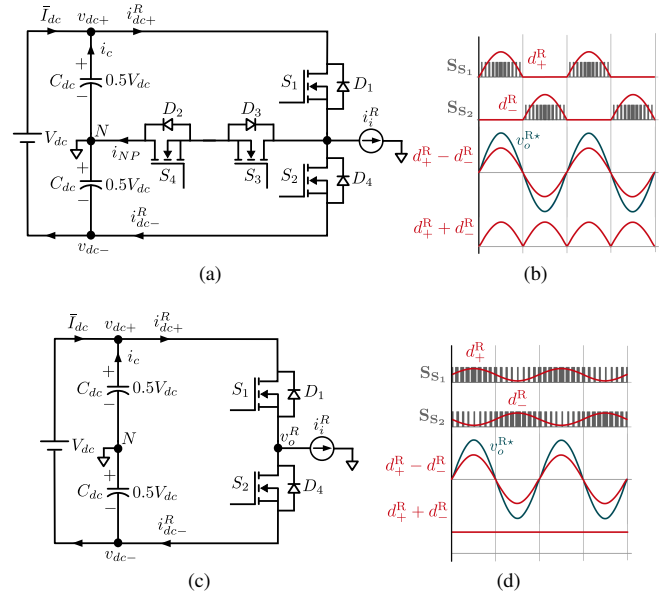


Fig. 1: Circuit schematic of PWM VSIs along with voltage reference, duty-ratio and switching functions of R-phase for (a)-(b) 3L-NPCI, and (c)-(d) traditional 2L-VSI.

2L-VSIs. For example, Fig. 2 compares the positive DC-link currents and voltages for the 3L- and 2L-VSI, and it can be seen from the current harmonic spectrum that there is considerable 3rd harmonic component, which is flowing in the DC-link via the neutral point ‘N’ of the 3L-NPCI. This causes a notable low-frequency 3rd harmonic NP-ripple on the DC-link voltages, as noted in v_{dc+} shown in Fig. 2(a). This NP-voltage ripple is common-mode (CM) (or zero-sequence) in nature appearing on both positive and negative DC-link voltages, and such a phenomena is absent in 2L-VSIs [10], as noted in Fig. 2(b). Although this NP-voltage variation characteristic is documented in 3L-NPCI literature [11]–[13], space-vector perspectives are almost exclusively employed for describing such a behavior, along with a qualitative treatment of its impact on the overall inverter performance. In particular, the low-frequency harmonic distortion observed in the 3L-NPCI output, is an aspect that is reported but not well characterized in literature [10], and therefore, requires further investigation and analytical quantification.

In this paper, we depart from investigations which are typically based on the space-vector approach, and adopt an

This material is based upon work supported by the U.S. Department of Energy’s Office of Energy Efficiency and Renewable Energy (EERE) under Solar Energy Technologies Office (SETO) Agreement Number EE0009025.

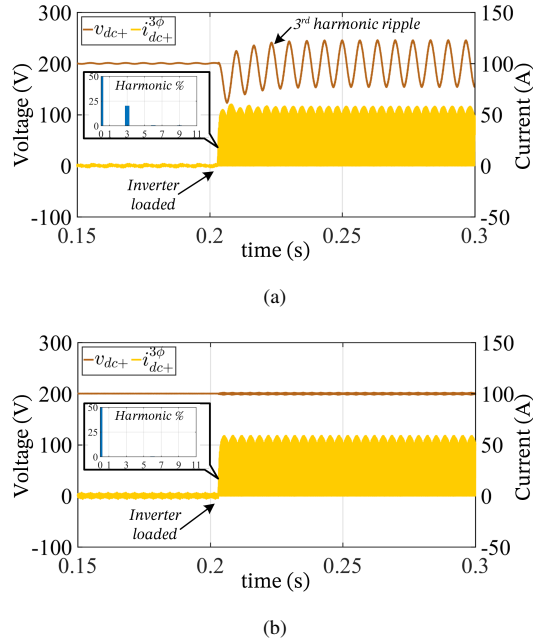


Fig. 2: Comparison of positive DC-link current and voltage for (a) 3L-NPCI showing the presence of 3rd-harmonic current component and corresponding ripple, and (b) 2L-inverter indicating the absence of 3rd-harmonic phenomena.

alternate Fourier-series based formulation to analyze the 3rd-harmonic phenomena and its impacts in the 3L-NPCI. We provide analytical investigations and quantification for: i) 3rd harmonic NP-current and corresponding NP-voltage ripple, and ii) translation of the CM NP-voltage ripple from the DC-side onto the AC-side as differential-mode (DM) voltage distortions that affect the inverter output voltage quality. Based on this quantitative analysis, we propose a model-based observer for nullifying the AC-side distortions by accurate estimation and cancellation of the same through feed-forward addition in the PWM reference generation scheme. Such an approach for harmonic compensation and improving output voltage quality is desirable due to its simplicity and ease of practical implementation. The quantitative results obtained in this paper are validated through a full-order switched model simulation in MATLAB[®]-Simulink. Major outcomes are also experimental verified on a 6 kW laboratory hardware prototype of a Silicon-Carbide (SiC) based 3L-NPC T-type inverter.

II. EVALUATION OF THIRD-HARMONIC NP-CURRENT

In this section, we begin with preliminaries on switching and averaged duty-ratio functions of the 3L-NPCI. Subsequently, we employ these time-domain functions to formulate the Fourier series description of the DC-link and compute the required 3rd NP-current.

A. Preliminaries

The circuit schematic of the R-phase leg in a three-phase 3L-NPC inverter is shown in Fig. 1(a), and to draw a contrast,

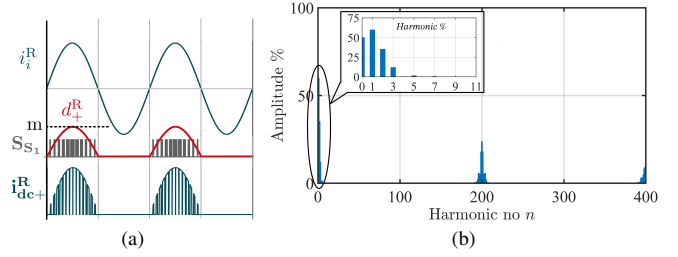


Fig. 3: (a) PDC-link current of R-phase and, (b) its frequency spectrum highlighting the presence lower order harmonics.

the schematic of the traditional 2L-VSI is shown in Fig. 1(c). For the 2L-case, the (well known) switching-cycle averaged PWM duty-ratios (d_+^R, d_-^R) for the top and bottom switches are continuous sine functions, given by:

$$d_+^R = \langle S_{S_1} \rangle_{T_s} = 0.5 + m \sin \theta, \quad d_-^R = \langle S_{S_2} \rangle_{T_s} = 0.5 - m \sin \theta,$$

where, (S_{S_1}, S_{S_2}) correspond to the PWM switching functions. On the other hand, for a 3L-inverter, due to the presence of a zero-state, the averaged PWM duty-ratios of the leg are discontinuous and time-shifted half-wave rectified-sine functions for all the typical carrier-based PWM techniques. For instance, for phase-disposition (PD)-PWM that is commonplace in 3L-PWM techniques, the reference duty ratios are given by:

$$d_+^R = \langle S_{S_1} \rangle_{T_s} = \begin{cases} m \sin \theta & 0 \leq \theta \leq \pi \\ 0 & \pi < \theta \leq 2\pi, \end{cases} \quad (1)$$

$$d_-^R = \langle S_{S_2} \rangle_{T_s} = \begin{cases} 0 & 0 \leq \theta < \pi \\ m \sin \theta & \pi \leq \theta \leq 2\pi. \end{cases} \quad (2)$$

The functions ($S_{S_1}, S_{S_2}, d_+^R, d_-^R$) for the main switches, for both 3L- and 2L-cases are shown in Fig. 1(b) and Fig. 1(d), respectively. Note that in case of the 3L-NPCI, the switching functions for the NP switches (S_{S_3}, S_{S_4}) are complementary to (S_{S_1}, S_{S_2}).

To evaluate the NP-current in a three-phase 3L-NPCI, the reflection of the AC-side load-current on the DC-side as a pulsed DC-link current is first analyzed. Both the positive-DC-link (PDC-link) and negative-DC-link (NDC-link) currents are pulsed and discontinuous in nature due to the switching action of the inverter. These are denoted as i_{dc+}^R and i_{dc-}^R , respectively. Since the two currents are symmetrical but flow in opposite directions, it is sufficient to analyze only i_{dc+}^R for the purpose of quantitative evaluation.

B. DC-link Current Evaluation

Let i_i^R be the R-phase load current, I_m be the peak value, $\theta = \omega t$ be the instantaneous phase, and ϕ be the load power-factor angle, such that,

$$i_i^R = I_m \sin(\omega t - \phi). \quad (3)$$

The pulsed PDC-link current i_{dc+}^R is defined with the aid of the switching function S_{S_1} (see Fig. 3(a) for visualization) as follows,

$$i_{dc+}^R = i_i^R S_{S_1}. \quad (4)$$

Averaging the above over the switching period T_s and using the definition in (1), we obtain the definition of averaged PDC-link current i_{dc+}^R :

$$i_{dc+}^R = i_i^R d_+^R. \quad (5)$$

To obtain the frequency components of the above, the Fourier spectrum of d_+^R , which is a half-wave-rectified sine function, is evaluated:

$$d_+^R = \frac{m}{\pi} + \frac{m}{2} \sin \theta - \sum_{n=2,4,\dots}^{\infty} \frac{2m}{\pi(n^2-1)} \cos n\theta. \quad (6)$$

From (3), (5), and (6) we get,

$$\begin{aligned} i_{dc+}^R &= \frac{mI_m}{\pi} \sin(\theta-\phi) + \frac{mI_m}{2} \sin \theta \sin(\theta-\phi) \\ &- \sum_{n=2,4,\dots}^{\infty} \frac{2mI_m}{\pi(n^2-1)} \cos n\theta \sin(\theta-\phi) \\ &= \frac{mI_m}{\pi} \sin(\theta-\phi) + \frac{mI_m}{4} [\cos \phi - \cos(2\theta-\phi)] \\ &- \sum_{n=2,4,\dots}^{\infty} \frac{2mI_m}{\pi(n^2-1)} \cos n\theta \sin(\theta-\phi). \end{aligned} \quad (7)$$

The above yields the complete Fourier series of the R-phase PDC-link current. The expression indicates the presence of DC, fundamental, 2nd, and other harmonic components. Figure 3(b) illustrates the frequency spectra of i_{dc+}^R , thereby verifying the result in simulation. Since n in (7) takes only even values, the product of the summation term with fundamental yields only odd harmonic components. In particular, $n = 2, 4$ leads to 3rd harmonic content in the DC-link current, which is evaluated as follows,

$$\begin{aligned} i_{dc+,3}^R &= -\frac{2mI_m}{3\pi} \cos 2\theta \sin(\theta-\phi) - \frac{2mI_m}{15\pi} \cos 4\theta \sin(\theta-\phi) \\ &= -\frac{mI_m}{3\pi} (\sin(3\theta-\phi) - \sin(\theta+\phi)) \\ &- \frac{mI_m}{15\pi} (\sin(5\theta-\phi) - \sin(3\theta+\phi)) \\ &= -\frac{mI_m}{3\pi} \left(\frac{4}{5} \sin 3\theta \cos \phi - \frac{6}{5} \cos 3\theta \sin \phi \right). \end{aligned}$$

Simplification of the above leads to the following general form,

$$i_{dc+,3}^R = \sqrt{2}I_3 \sin(3\theta - \alpha_3), \quad (8)$$

where, I_3 and α_3 above represent the RMS magnitude and phase of the 3rd harmonic current on the DC-side, respectively, given by:

$$I_3 = -\frac{\sqrt{2}mI_m}{5\pi} \sqrt{1 - \frac{5}{9} \cos^2 \phi}, \quad (9a)$$

$$\alpha_3 = \tan^{-1} \left(-\frac{3}{2} \tan \phi \right). \quad (9b)$$

Using the developments above, we next evaluate the NP-current in a 3L-NPCI.

C. NP-Current Evaluation in Three-phase Case

For a three-phase 3L-NPCI, the DC and 3rd (or triplen) harmonic components on the DC-side contributed by individual phases, are zero-sequence in nature and hence add up algebraically. The remaining harmonics for $n \in [1, 2, 5, 7, \dots]$, on the other hand, are either positive or negative sequence components which are balanced in the three-phase sense, and hence, sum up to zero. While the average DC-link current is a differential-mode component supplied completely by the front-end system feeding the DC-link, the 3rd (and other triplen) harmonic currents are common-mode components flowing into the DC-link capacitors through the neutral point.

Remark-1: The 3rd harmonic phenomena on the DC-side is therefore noted to be a direct consequence of the nature of the average duty-ratio wave-shape and its product with the inverter pole current.

The total PDC-link current for the three-phase case can be written as the sum of the contributions of the individual phases:

$$i_{dc+}^{3\phi} = i_{dc+}^R + i_{dc+}^Y + i_{dc+}^B. \quad (10)$$

The RMS value of the 3rd harmonic component in $i_{dc+}^{3\phi}$, denoted as $I_{dc+,3}^{3\phi}$, is equal to thrice that of the R-phase 3rd harmonic component obtained in (9a), i.e. $I_{dc+,3}^{3\phi} = 3I_3$, and its phase is equal to that in (9b). This component flows through the PDC-link capacitor and causes a ripple in v_{dc+} ; an equal amount of current flows through the NDC-link capacitor contributed by the NDC-link current $i_{dc-}^{3\phi}$. As a result, the total NP-current is constituted by sum of 3rd harmonic current contributions from both PDC- and NDC-link currents, which are equal in magnitude and phase. This can be expressed as:

$$I_{NP} = 2I_{dc+,3}^{3\phi} = 6I_3 = \frac{6\sqrt{2}mI_m}{5\pi} \sqrt{1 - \frac{5}{9} \cos^2 \phi}, \quad (11a)$$

$$\alpha_{NP} = \alpha_3. \quad (11b)$$

Equation (11) yields the total RMS magnitude I_{NP} and phase α_{NP} of the neutral-point current in a 3L-NPCI. For visualization, its variation as a function of operating modulation index and power-factor is shown as a surface plot (normalized with rated RMS load current I_o^R) in Fig. 4. It can be seen that maximum modulation index and zero pf load forms the worst case scenario causing about 80% of 3rd harmonic current flow on the DC-side. Note that the result in (11), is generalized and applicable for all the typical carrier based PWM techniques such as in-phase and phase-opposition PWM.

III. IMPACT ANALYSIS ON DC SIDE

The 3rd harmonic NP-current impacts the DC-link in two ways: i) 3rd-harmonic NP common-mode voltage ripple is caused on the DC-link voltage, and ii) excess power loss is incurred in the DC-link capacitors. Analytical treatment of these impacts are presented next.

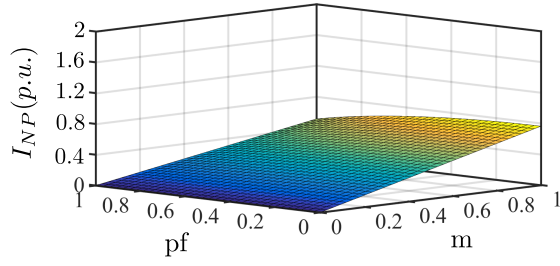


Fig. 4: Surface plot showing the variation of RMS magnitude of 3rd harmonic DC-link current based on (11a).

A. NP-voltage Ripple Evaluation

The CM current $i_{dc+,3}$ on the DC side causes a CM voltage ripple on the DC capacitors. To compute this, we first obtain the impedance of the capacitor. Let C_{dc} and $r_{esr}(f)$ be the capacitance and frequency dependent equivalent-series-resistance (ESR) of the DC-link capacitor, respectively. The capacitive impedance at the 3rd harmonic frequency is $Z_c(j\omega_3) = r_{esr}(f_3) + (j\omega_3 C_{dc})^{-1}$; $|Z_c(j\omega_3)|$ and β_3 , denote the corresponding magnitude and phase of this impedance, respectively, and they are given by:

$$|Z_c(j\omega_3)| = \sqrt{r_{esr}^2(f_3) + \frac{1}{\omega_3^2 C_{dc}^2}}, \quad (12a)$$

$$\beta_3 = \tan^{-1} \left(\frac{-1}{\omega_3 C_{dc} r_{esr}(f_3)} \right). \quad (12b)$$

The instantaneous NP-voltage ripple can be evaluated using (11) and (12) as:

$$\tilde{v}_{cm} = \sqrt{2} \tilde{V}_{cm} \sin(3\theta - \alpha_{NP} - \beta_3), \quad (13a)$$

$$\tilde{V}_{cm} = 0.5 I_{NP} |Z_c(j\omega_3)|, \quad (13b)$$

where, \tilde{V}_{cm} represents the RMS NP-voltage ripple. Figure 2(a) shows the simulated PDC-capacitor voltage v_{dc+} indicating the NP-ripple in a 3L-NPCI, and contrasts the same with a 2L-VSI where such a NP-voltage oscillation is absent.

B. DC-capacitor Power Loss

The equivalent-series-resistance (ESR) of a DC capacitor $r_{esr}(f)$ is a nonlinear parameter that varies as a function of operating frequency. Its magnitude at f_1 can be significantly higher than that at f_{sw} [14]. The specific values at the two frequencies can be obtained from the capacitor datasheets. Let the average and RMS values of the DC-link current be denoted as I_{dc+} and \bar{I}_{dc+} , respectively, (see Appendix for expressions), the power loss incurred in the DC capacitor can be estimated with improved accuracy, as follows,

$$P_{loss} = 0.25 I_{NP}^2 r_{esr}(3f_1) + \left[\left(\bar{I}_{dc+}^{3\phi} \right)^2 - \left(\bar{I}_{dc+} \right)^2 - 0.25 I_{NP}^2 \right] r_{esr}(f_{sw}). \quad (14)$$

IV. IMPACT ANALYSIS ON AC-SIDE

The main impact of the 3rd harmonic NP-current is the translation of the common-mode NP-voltage ripple from the DC side onto the AC side as differential-mode (DM) voltage distortions, affecting the inverter output voltage quality. This translation is analyzed and the corresponding distortion is quantified in this section.

A. Evaluation of AC Output Distortions

Let the positive and negative DC-link voltages, including the ripple as disturbance, be represented in the following generalized form as,

$$v_{dc+} = \frac{V_{dc}}{2} + \frac{\tilde{v}_{dm}}{2} + \tilde{v}_{cm}, \quad v_{dc-} = -\frac{V_{dc}}{2} - \frac{\tilde{v}_{dm}}{2} + \tilde{v}_{cm}, \quad (15)$$

where, \tilde{v}_{cm} and \tilde{v}_{dm} represent the CM and DM ripple components on the DC-link. The averaged inverter pole voltage v_o^R can be written using the above as:

$$v_o^R = \left(\frac{V_{dc}}{2} + \frac{\tilde{v}_{dm}}{2} \right) (d_+^R - d_-^R) + \tilde{v}_{cm} (d_+^R + d_-^R). \quad (16)$$

From (16), it is observed that both the DC-side ripple components get translated to the AC-side through the (product with) duty-ratio functions. From the 3L duty-ratio definitions in (1) and (2), the difference and sum of the duty-ratio functions (illustrated in Fig. 1(b)) are given by:

$$d_+^R - d_-^R = m \sin \theta, \quad d_+^R + d_-^R = m |\sin \theta|. \quad (17)$$

Using (13) and the above result in (16), we get:

$$v_o = \frac{V_{dc}}{2} m \sin \theta + \underbrace{\frac{\tilde{v}_{dm}}{2} m \sin \theta + \tilde{v}_{cm} m |\sin \theta|}_{\tilde{v}_o^R}. \quad (18)$$

The above yields the generalized averaged output-voltage expression for a 3L-NPCI, showing the manner in which both the common-and differential-mode voltage ripple components on the DC-side get translated to the AC-side. The first term in (18) denotes the desired fundamental output voltage, while the second, \tilde{v}_o^R , represents the undesirable distortion.

Remark-2: In a 3L-NPCI, both the averaged duty-ratio functions and DC-side ripple voltages are time-varying quantities, and hence, their product corresponds to a nonlinear operation in the system that introduces additional harmonic frequencies at the inverter output.

If the DC-bus is fed by a stiff source, the DM-ripple would be almost zero, i.e., $\tilde{v}_{dm} = 0$. Using this, and expanding \tilde{v}_o in a Fourier series, we get:

$$\begin{aligned} \tilde{v}_o^R &= \tilde{v}_{cm} \frac{2m}{\pi} - \sum_{n=2,4,\dots}^{\infty} \frac{4m\tilde{v}_{cm}}{\pi(n^2-1)} \cos n\theta \\ &= \frac{2\sqrt{2}}{\pi} m \tilde{V}_{cm} \sin(3\theta - \alpha_3 - \beta_3) \\ &\quad + \frac{4\sqrt{2}m\tilde{V}_{cm}}{\pi} \sum_{n=2,4,\dots}^{\infty} \frac{\cos n\theta}{(n^2-1)} \sin(3\theta - \alpha_3 - \beta_3). \end{aligned} \quad (19)$$

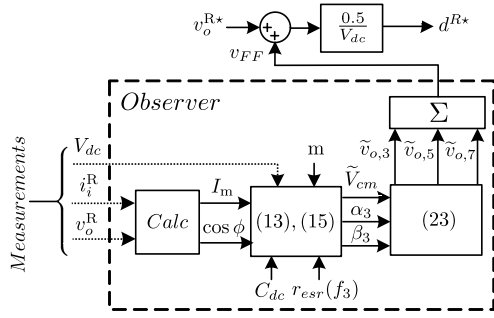


Fig. 5: Model based observer structure for harmonic compensation through feed-forward addition.

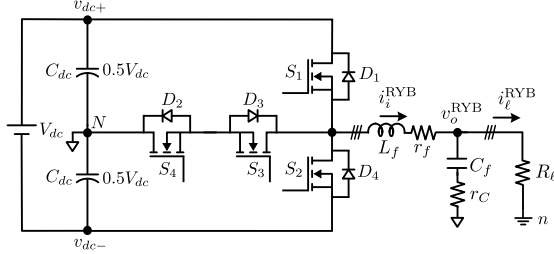


Fig. 6: Circuit schematic of standalone three-phase 3L-NPCI under open-loop operation showing LC-filter L_f, C_f and load resistance R_ℓ .

From the above, it can be noted that the first term contributes to the 3rd harmonic component at the inverter output. Since n takes even values only, the second summation term, which corresponds to the product operation with 3rd harmonic, thus, causes additional odd harmonics at the output. For example, $n = 2, 4$ above leads to the 5th and 7th harmonic components in the AC output.

Remark-3: In a 3L-NPCI, the common-mode 3rd harmonic NP-voltage ripple gets translated as differential-mode lower-order odd-harmonic voltage distortions at the AC output, resulting in voltage quality degradation.

The major odd-harmonic components at the R-phase output are evaluated as,

$$\tilde{v}_{o,3}^R = \frac{2m}{\pi} \sqrt{2} \tilde{V}_{cm} \sin(3\theta - \alpha_3 - \beta_3), \quad (20a)$$

$$\tilde{v}_{o,5}^R = \frac{2m}{3\pi} \sqrt{2} \tilde{V}_{cm} \sin(5\theta - \alpha_3 - \beta_3), \quad (20b)$$

$$\tilde{v}_{o,7}^R = \frac{2m}{15\pi} \sqrt{2} \tilde{V}_{cm} \sin(7\theta - \alpha_3 - \beta_3). \quad (20c)$$

The harmonic distortions in Y- and B-phases can be computed in a similar fashion.

B. Mitigation Technique

The low-frequency harmonic distortions in the 3L-NPCI AC output can be mitigated in multiple ways. One method is to scale up the DC-capacitance sufficiently high and diminish the NP-voltage ripple magnitude. However, in order to enhance the overall system reliability, it is often desirable to keep the DC-link slim and use film capacitors [15]. In high-power converters

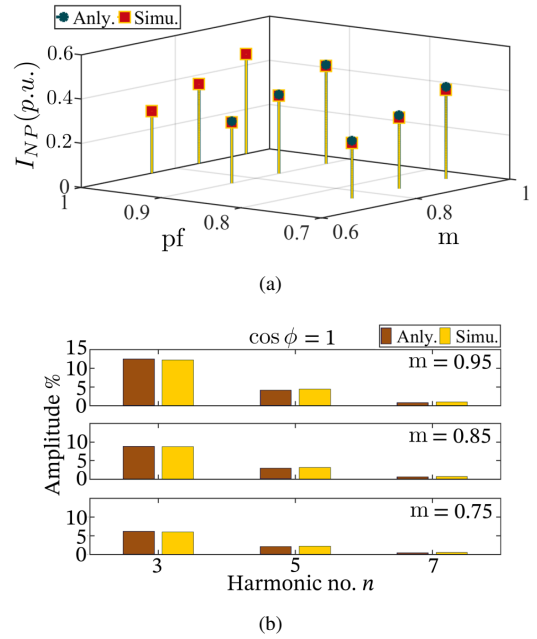


Fig. 7: (a) Stem-plot of 3rd harmonic NP-current comparing analytical and simulation RMS values for different m and pf values, (b) Bar-chart comparing analytical and simulated RMS magnitudes of dominant 3rd, 5th, and 7th harmonics in the AC output voltage.

where the switching frequency f_s is typically restricted, the control-loop bandwidths are inadequate to reject the AC-side harmonic distortions, and hence, cannot be relied upon for disturbance-rejection. In systems where the plant disturbances are deterministic and can be modeled analytically, a feed-forward addition at an appropriate location in the control system is often the method of choice for countering the disturbance inputs. For instance, in grid-tied inverter systems, it is common to employ feed-forward cancellation to counter the grid-voltage and the cross-coupling (frequency-current product) terms in the control-loop [16], [17]. Since the 3L-NPCI lends itself for disturbance-modeling as shown in Section IV, the feed-forward approach is adopted in this paper. It is noteworthy that the duty-ratio command generation by dividing the voltage-reference with measured DC-link voltage V_{dc} , as is typically done in the 2L-VSI case, will not solve the problem of harmonic distortions, as the root-cause is common-mode in nature. Hence, a model-based observer is designed based on (11), (13), and (20), to accurately estimate and cancel the disturbance in question. The block schematic of the observer is shown in Fig. 7(b), where, V_{dc} , v_o^R and i_i^R are measured signals from hardware. The computation block 'Calc' calculates the current peak I_m and pf from the measurements, and subsequently, the observer computes the required feed-forward compensation term v_{FF}^R as below:

$$v_{FF}^R = -(\tilde{v}_{o,3}^R + \tilde{v}_{o,5}^R + \tilde{v}_{o,7}^R). \quad (21)$$

This is added to the voltage-reference signal v_o^{R*} and the resultant duty-ratio command d^{R*} is employed to generate the

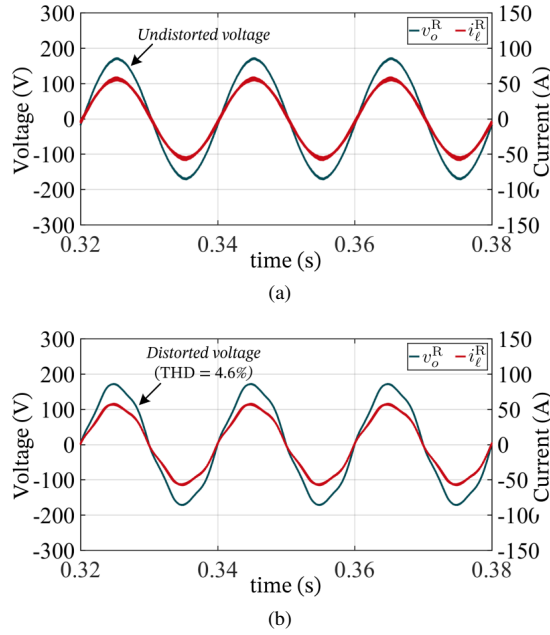


Fig. 8: Comparison of profiles of load current i_l^R and output capacitor voltage v_o^R along with its THD for (a) 2L-VSI, and (b) 3L-NPCI.

PWM pulses for the 3L-NPCI. Similar feed-forward addition and compensation is carried out in Y- and B-phases as well. It is worth noting that the measurements errors (in voltage and current inputs of the observer) have a direct impact on the accuracy of harmonic compensation and quantum of voltage quality improvement that can be achieved.

V. RESULTS AND DISCUSSION

In this section, simulation and experimental results are presented that substantiate the theoretical analysis. Fig. 6 shows the circuit schematic of a three-phase 15 kW, 120 V, 3L-NPCI in standalone configuration employed for validation. It consists of DC-capacitance $C_{dc} = 300 \mu F$, output LC-filter ($L_f = 1 mH$, $C_f = 47 \mu F$), and load resistance R_l . The inverter is operated with $V_{dc} = 400 V$ at a switching frequency of $f_s = 10 kHz$ for the simulation and experiment.

A. Simulation

A full-order switched model simulation of the 3L-NPCI shown in Fig. 6 is carried out in MATLAB®- Simulink, under open-loop operation. Figure 7(c) presents a stem-plot comparing the normalized (with rated load current I_l^R) magnitudes of NP-current in (11a) with that obtained from simulation, for a set of discrete operating conditions of modulation index, m, and power factor, pf. The overlap of the respective stems in all the test cases indicates a close match between the two data-sets validating the analysis presented in Section II. A bar-chart is presented in Figure 7(b) that compares the dominant odd-harmonics' magnitudes of ($n = 3, 5, 7$) present on the AC output based on (20), with that observed in simulation. In this case as well, a close match is seen between the two

TABLE I: Comparison of percentage magnitudes of simulated and measured DC- and AC-side harmonic distortion components in 3L-NPCI.

Harmonic component	Simulation (%)	Experiment (%)	Error (%)
\tilde{V}_{cm}	5.4	4.6	-10.2
$\tilde{V}_{o,3}^R$	9.5	8.5	-11.7
$\tilde{V}_{o,5}^R$	3.5	3.1	-12.9
$\tilde{V}_{o,7}^R$	0.83	0.75	-10.6

results validating the analysis presented in Section IV. In both figures, the observed RMS error (RMSE) is less than 2%, indicating the high accuracy of the derived analytical expressions. The translation of NP-oscillation into AC-side voltage distortions is further illustrated in Fig. 8, where the outputs of 3-phase standalone 2L- and 3L-VSI are compared under identical operating conditions. It can be seen that in a 2L-VSI, no distortions are observed on the AC output, as no NP-ripple exists on the DC-side, while for the 3L-case, noticeable distortions are present in the AC output which are undesirable. Figure 9(a) shows the performance of the observer in estimating the DC-link voltage v_{dc+} along with the 3rd harmonic component when the 3L-NPCI is operating at rated load. Accurate tracking performance can be noted after the observer is enabled, thus verifying the expression derived in (13). In Fig. 9(b), the AC output voltage and load current profiles are shown before and after enabling the observer action. It can be seen that the distorted AC output voltage with total harmonic distortion THD = 4.6% is corrected by the feed-forward action of the observer, improving the THD to 0.75%, and thus validating its performance as described in Section IV-B.

B. Experimental Validation

In this section, experimental results are presented illustrating the DC-side NP-ripple and AC-side voltage distortions of the inverter under open-loop operation. The hardware setup of the 3L-NPCI system is shown in Fig. 9(c). The inverter is loaded to 6 kW power level with $C_{dc} = 150 \mu F$ and $m = 0.82$, and the steady-state three-phase load currents i_l^{RYB} , filter capacitor voltages v_o^{RYB} , and the individual DC-link capacitor voltages v_{dc+} , v_{dc-} (observed in *ac-mode*) are shown in Fig. 10(a). The 3rd harmonic ripple in v_{dc+} and v_{dc-} are equal and opposite in nature, indicating the common-mode nature of the NP-oscillation. In Fig. 10(b), the distorted R-phase output voltage v_c^R of the 3L-NPCI is shown along with v_{dc+} and inverter and load currents i_i^R and i_l^R , respectively. The inverter current is seen to carry notable switching-frequency ripple, but the load current is ripple-free due to the action of LC-filter. The measured amplitudes of the 3rd harmonic NP-oscillation (normalized with V_{dc}) along with 3rd, 5th and 7th harmonic components in R-phase output AC voltage (normalized with 120 V) are compared with the simulation results in Table. I. It can be seen that the observed error between simulation and experiment is close to 10%, thus verifying the accuracy of the results in Section II-C and III-A. Figure 10(c) presents

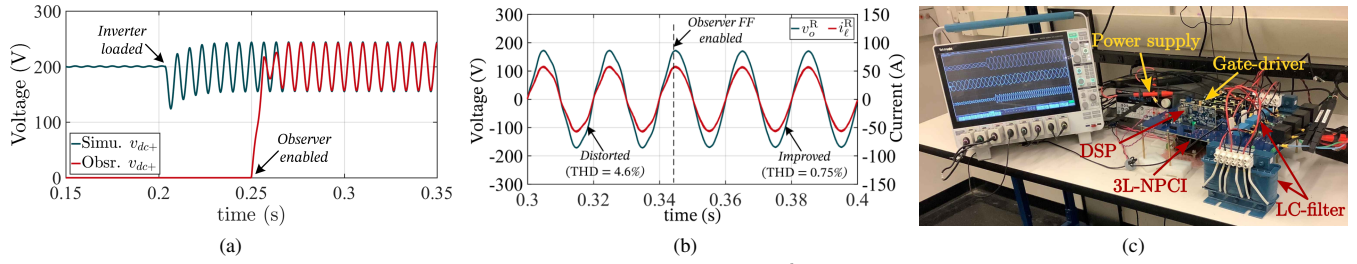


Fig. 9: (a) Performance of model-based observer showing tracking of 3rd harmonic DC-link voltage when enabled, (b) feed-forward compensation of AC output distortion after observer action is enabled, and (c) hardware prototype of 3L-NPCI.

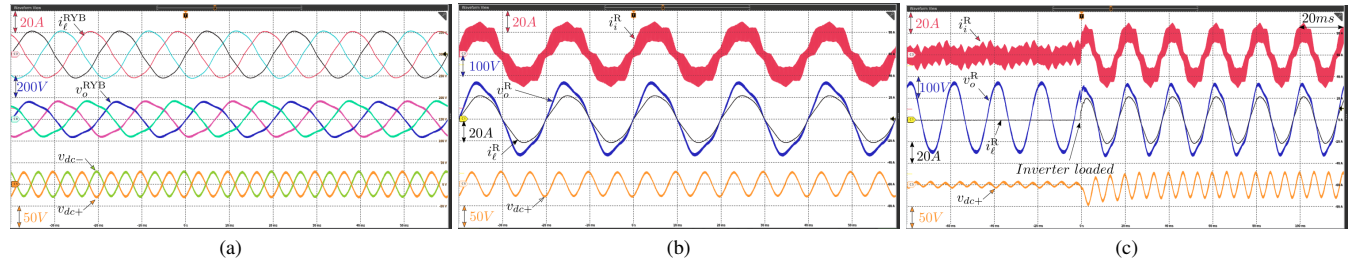


Fig. 10: Experimental open-loop performance of 3L-NPCI highlighting the 3rd harmonic DC-link voltage ripple and its impact, showing (a) three-phase line currents i_ℓ^{RYB} and capacitor voltages v_o^{RYB} , and DC-link voltages v_{dc+} and v_{dc-} in steady-state, (b) R-phase current and voltages i_ℓ^R , v_o^R and v_{dc+} in steady-state showing output voltage distortions, and (c) transient response of the inverter showing the increase of NP-ripple and inception of AC-side distortions after loading takes place.

the transient response of the inverter when the 6 kW load is applied. It can be observed that prior to the application of load, the magnitude of NP-ripple (as seen from v_{dc+}) is minimal, and hence, the filtered AC voltage v_o^R remains almost sinusoidal. After the application of load, the NP-ripple increases sharply due to its dependency on load current amplitude I_m , thus causing a notable degradation in the AC output voltage quality, as explained in Section IV. Thus, these experimental results together verify the major analytical results derived in this paper.

VI. CONCLUDING REMARKS

In this paper, the 3rd-harmonic neutral-point current flowing in 3L-NPC inverter is analyzed using time-domain formulations and Fourier-series expansions. The DC-side NP-voltage ripple is analytically evaluated and its impact on DC-link capacitor loss as well as the mechanism of its translation onto the inverter AC-side as differential-mode lower-order harmonics are quantitatively analyzed. Using this, a model-based observer is designed that measures the load current and accurately estimates the distortion components. This is used to compensate AC-side distortions through feed-forward cancellation, thus improving the output voltage quality. A full-order switched model simulation in Matlab-Simulink verifies the accuracy of the quantitative analysis and the performance of the observer. Experimental results on a 6 kW SiC based 3L-NPCI operating in standalone mode validate the theoretical results on 3rd NP voltage ripple and the corresponding degradation in inverter voltage-output quality.

APPENDIX

The average DC value of the PDC-link current $\bar{I}_{dc+}^{3\phi}$ (evaluated over the fundamental period T_1) in the 3L-NPCI is obtained from (7) and (10), given by:

$$\bar{I}_{dc+}^{3\phi} = \langle i_{dc+}^{3\phi} \rangle_{T_1} = 3 \langle i_{dc+}^R \rangle_{T_1} = \frac{3}{4} m I_m \cos \phi. \quad (22)$$

The RMS value of the PDC-link current $I_{dc+}^{3\phi}$ is given by:

$$I_{dc+}^{3\phi} = I_m \sqrt{\frac{\sqrt{3}m}{4\pi} + \cos^2 \phi \left(\frac{\sqrt{3}m}{\pi} - \frac{9m^2}{16} \right)}. \quad (23)$$

REFERENCES

- [1] H. Ghoddami and A. Yazdani, "A mitigation strategy for temporary overvoltages caused by grid-connected photovoltaic systems," *IEEE Trans. Energy Convers.*, vol. 30, no. 2, pp. 413–420, 2015.
- [2] V. Purba, B. B. Johnson, S. Jafarpour, F. Bullo, and S. V. Dhople, "Dynamic aggregation of grid-tied three-phase inverters," *IEEE Trans. Power Sys.*, vol. 35, no. 2, pp. 1520–1530, 2020.
- [3] V. Purba, B. B. Johnson, and S. V. Dhople, "Reduced-order aggregate model for parallel-connected grid-tied three-phase photovoltaic inverters," in *Proc. IEEE 46th Photovoltaic Specialists Conf. (PVSC)*, 2019, pp. 0724–0729.
- [4] D. Venkatramanan and V. John, "A reconfigurable solar photovoltaic grid-tied inverter architecture for enhanced energy access in backup power applications," *IEEE Trans. Ind. Electron.*, vol. 67, no. 12, pp. 10531–10541, 2020.
- [5] P. Roja, D. Venkatramanan, and V. John, "Design considerations of ultracapacitor stack for optimal sizing of energy storage systems in contingency applications," *IEEE Trans. Ind. Appl.*, vol. 56, no. 6, pp. 6803–6814, 2020.

- [6] L. Masisi, P. Pillay, and S. S. Williamson, "A Three-Level Neutral-Point-Clamped Inverter Synchronous Reluctance Machine Drive," *IEEE Trans. Ind. Appl.*, vol. 51, no. 6, pp. 4531–4540, 2015.
- [7] A. Anthon, Z. Zhang, M. A. Andersen, D. G. Holmes, B. McGrath, and C. A. Teixeira, "The benefits of SiC mosfets in a T-type inverter for grid-tie applications," *IEEE Trans. Power Electron.*, vol. 32, no. 4, pp. 2808–2821, 2017.
- [8] Z. Zhao, Y. Zhong, H. Gao, L. Yuan, and T. Lu, "Hybrid selective harmonic elimination PWM for common-mode voltage reduction in three-level neutral-point-clamped inverters for variable speed induction drives," *IEEE Trans. Power Electron.*, vol. 27, no. 3, pp. 1152–1158, 2012.
- [9] S. Das, G. Narayanan, and M. Pandey, "Space-vector-based hybrid pulsewidth modulation techniques for a three-level inverter," *IEEE Trans. Power Electron.*, vol. 29, no. 9, pp. 4580–4591, 2014.
- [10] A. Bendre, S. Krstic, J. Vander Meer, and G. Venkataramanan, "Comparative evaluation of modulation algorithms for neutral-point-clamped converters," *IEEE Trans. Ind. Appl.*, vol. 41, no. 2, pp. 634–643, 2005.
- [11] J. Zaragoza, J. Pou, S. Ceballos, E. Robles, C. Jaen, and M. Corbalán, "Voltage-balance compensator for a carrier-based modulation in the neutral-point-clamped converter," *IEEE Trans. Ind. Electron.*, vol. 56, no. 2, pp. 305–314, 2009.
- [12] J. Pou, J. Zaragoza, P. Rodríguez, S. Ceballos, V. M. Sala, R. P. Burgos, and D. Boroyevich, "Fast-processing modulation strategy for the neutral-point-clamped converter with total elimination of low-frequency voltage oscillations in the neutral point," *IEEE Trans. Ind. Electron.*, vol. 54, no. 4, pp. 2288–2294, 2007.
- [13] C. Wang and Y. Li, "Analysis and calculation of zero-sequence voltage considering neutral-point potential balancing in three-level NPC converters," *IEEE Trans. Ind. Electron.*, vol. 57, no. 7, pp. 2262–2271, 2010.
- [14] M. Gasperi, "Life prediction modeling of bus capacitors in ac variable-frequency drives," *IEEE Trans. Ind. Appl.*, vol. 41, no. 6, pp. 1430–1435, 2005.
- [15] P. Alemi, Y. C. Jeung, and D. C. Lee, "DC-Link capacitance minimization in T-type three-level AC/DC/AC PWM converters," *IEEE Trans. Ind. Electron.*, vol. 62, no. 3, pp. 1382–1391, 2015.
- [16] D. Venkataramanan and V. John, "Dynamic phasor modeling and stability analysis of SRF-PLL-based grid-tie inverter under islanded conditions," *IEEE Trans. Ind. Appl.*, vol. 56, no. 2, pp. 1953–1965, 2020.
- [17] X. Zhang, D. Xia, Z. Fu, G. Wang, and D. Xu, "An improved feedforward control method considering PLL dynamics to improve weak grid stability of grid-connected inverters," *IEEE Trans. Ind. Appl.*, vol. 54, no. 5, pp. 5143–5151, 2018.